EUMETSAT Contract No. EUM/CO18/4600002180/JML

EVOLUTIONS STUDIES AUTOMATED OPTICAL SENSOR REGISTRATION MONITORING TOOL

Study Report

Deliverable D17

Prepared by

Stefan SCHEIBLAUER and Thomas NAGLER

ENVEO IT, Innsbruck, AUSTRIA

Document Reference: ENVEO-OSMON_D17.SR
Issue / Revision: 1 / 0
Date: 17.09.2020

Document controlled by Stefan Scheiblauer

EUMETSAT STUDY CONTRACT REPORT

CONTRACT NO:	**SUBJECT:**		**CONTRACTOR:**
EUM/CO18/4600002180/JML	Deliverable D17 - Study Report		ENVEO
	STAR CODE:	**NO OF VOLUMES**: 1 **THIS IS VOLUME NO**: 1	**CONTRACTOR'S REF:** Deliverable D17

ABSTRACT:

Precise geolocation of satellite imagery is fundamental for systematic climate observations. It allows multi-sensor composites and long-term time series of Essential Climate Variables (ECVs). The World Meteorological Organization (WMO) has summarized baseline requirements for satellite-based climate products in (GCOS 2006). It requires for moderate-resolution optical instruments a geolocation accuracy better than 1/3 of the instantaneous field of view (IFOV) in the terrestrial domain.

The project "OSMON - Automated Optical Sensor Registration Tool" is a platform-independent modular software tool for assessing and monitoring the geolocation accuracy of medium to high resolution optical sensors. The tool supports Level-1 products from current medium resolution (MROI) EUMETSAT sensors AVHRR, SLSTR and OLCI and is extendable to near-future sensors. An iterative area-based cross-correlation method was implemented to estimate the shift between Landsat-8 NIR and TIR bands and MROI-DataWindows (MROI-DW).

Short time gaps between observed and reference images for shift estimates in thermal bands are critical. This challenge can be addressed by extending the reference dataset with seasonal reference images as well as night reference images. Further, upcoming sensors provide an opportunity for monitoring of climate variables and therefore it is made possible to include this suite of sensors to the OSMON-software.

With OSMON an easy-to-use software tool was created to evaluate and plot geolocation accuracy. This report summarizes the findings encountered during the development of the OSMON software package focusing on the shift estimation module.

The work described in this report was done under EUMETSAT Contract. Responsibility for the contents resides in the authors or organization that prepared it.

AUTHORS:
STEFAN SCHEIBLAUER AND THOMAS NAGLER

EUMETSAT STUDY MANAGER:	**EUMETSAT BUDGET HEADING**
Johannes Müller	

DOCUMENT CHANGE LOG

Issue/ Revision	Date	Modification	Modified pages	Observations
1.0	17.09.2020	All new	All	NA

TABLE OF CONTENT

APPLICAPLE AND REFERENCE DOCUMENTS

[RD-1]	ENVEO IT, (2019), Evolution Studies - Automated Optical Sensor Registration Monitoring Tool. Algorithm Theoretical Basis Document, Deliverable D08 ENVEO-OSMON_D08.ATBD_1/5
[RD-2]	Django Software Foundation, Django (web framework). https://djangoproject.com, 2019
[RD-3]	Guizar-Sicairos, M., Thurman, S. T. and Fienup, J. R. (2008) 'Efficient subpixel image registration algorithms', Optics Letters, 33(2), p. 156. doi: 10.1364/OL.33.000156.
[RD-4]	ENVEO IT, (2019), Evolution Studies - Automated Optical Sensor Registration Monitoring Tool. State of the Art, Deliverable D04, ENVEO-OSMON_D12.PVR_1/2
[RD-5]	ENVEO IT, (2019), Evolution Studies - Automated Optical Sensor Registration Monitoring Tool. Output data format and Reference data set Deliverable D09/D10/D11 ENVEO-OSMON_D09_D10_11.ODF_RDB_DDS_1/0
[RD-6]	J. P. W. Pluim, J. B. A. Maintz, und M. A. Viergever, „Mutual-information-based registration of medical images: a survey", IEEE Trans. Med. Imaging, Bd. 22, Nr. 8, S. 986–1004, Aug. 2003, doi: 10.1109/TMI.2003.815867.
[RD-7]	S. Van der Walt u. a., „scikit-image: image processing in Python", PeerJ, Bd. 2, S. e453, 2014.
[RD-8]	GCOS, „Systematic observation requirements for satellite-based products for climate-Supplemental details to the satellite-based component of the "Implementation Plan for the Global Observing System for Climate in Support of the UNFCCC"", Technical Report GCOS-107, WMO/TD No 1338, 2006.
[RD-9]	A. Gerace und M. Montanaro, „Derivation and validation of the stray light correction algorithm for the thermal infrared sensor onboard Landsat 8", Remote Sensing of Environment, Bd. 191, S. 246–257, 2017.

Note: If not provided, the reference applies to the latest released Issue/Revision/Version

ACRONYMS

3MI ..... *Multi-Viewing Multi-Channel Multi-Polarisation Imaging*
AVHRR ..... *Advanced Very High Resolution Radiometer*
DW ..... *Data Window*
FCI ..... *Flexible Combined Imager*
GCP ..... *Ground Control Point*
IFOV ..... *Instantaneous Field of View*
MetOp ..... *Meteorological Operational Satellite*
MetOp-SG ..... *MetOp-Second Generation*
MI ..... *Mutual Information*
MROI ..... *Medium Resolution Optical Imager*
MTG ..... *Meteosat Third Generation*
NIR ..... *Near Infrared*
OLCI ..... *Ocean and Land Colour Instrument*
OLI ..... *Operational Land Imager*
SLSTR ..... *Sea and Land Surface Temperature Radiometer*
SNR ..... *Signal-to-noise ratio*
SWIR ..... *Shortwave Infrared*
TIR ..... *Thermal Infrared*
TIRS ..... *Thermal Infrared Sensor*
VIS ..... *Visible*
WMO ..... *World Meteorological Organization*

DEFINITION OF TERMS

GCP	**In the OSMON project the term Ground Control Point (GCP) refers to an image template covering a prominent feature on the Earth Surface, which can be identified in medium resolution optical images. GCP image templates are extracted from VIS, NIR, SWIR, TIR spectral bands of Landsat-8 OLI and TIRS data. The geographic location of a GCP is exactly specified by the geographic map projection, ellipsoid and local datum, corner coordinates and pixel spacing in Easting and Northing direction.**
MROI	Medium Resolution Optical Imagers is used as a general name of medium resolution optical satellites such as Sentinel-3 SLSTR, Sentinel-3 OLCI and MetOp/AVHRR.
MROI-DW	This term is used for MROI-satellite data covering the same area as the corresponding GCP.MROI-DW are raster files in the same map projection, ellipsoid and local datum, corner coordinates and pixel spacing in Easting and Northing direction. To achieve the same pixel spacing as GCP, oversampling of the native resolution of the MROI data is applied.

1. INTRODUCTION

Precise geolocation of satellite imagery is fundamental for systematic climate observations. It allows multi-sensor composites and long-term time series of Essential Climate Variables (ECVs). The World Meteorological Organization (WMO) has summarized baseline requirements for satellite-based climate products in [RD-8]. It requires for moderate-resolution optical instruments a geolocation accuracy better than 1/3 of the instantaneous field of view (IFOV) in the terrestrial domain.

The project "OSMON - Automated Optical Sensor Registration Tool" is a platform-independent modular software tool for assessing and monitoring the geolocation accuracy of the medium to high resolution optical sensors. The tool supports Level-1 products from the current medium resolution (MROI) EUMETSAT sensors AVHRR, SLSTR and OLCI and is extendable to near-future sensors. For the shift estimation, an iterative area-based cross-correlation method was selected to match Landsat-8 NIR and TIR bands against MROI-DataWindows (MROI-DW).

For the year 2017 AVHRR3 (NIR and TIR) datasets show shifts smaller 1/3 pixel in North-South direction whereas in East-West Direction shifts exceed 1/3 pixel. For all other sensors (NIR and TIR), a component wise geolocation accuracy within the required 1/3 pixel was found.

Short time gaps between observed and reference images for shift estimates in thermal bands are critical. This challenge can be addressed by extending the reference dataset with seasonal reference images as well as night reference images. Further, upcoming sensors provide an opportunity for monitoring of climate variables and therefore it is made possible to include this suite of sensors to the OSMON-software.

With OSMON an easy to use software tool was created to evaluate and plot geolocation accuracy. This report summarizes the findings encountered during the development of the OSMON software package focusing on the matching module.

2. HIGH LEVEL SOFTWARE ARCHITETURE

The OSMON geolocation assessment tool has a modular design and consists of a ***Core Module*** and a ***Reporting and Analysis Module*** (Figure 1) implemented in Python's Django framework [RD-2].

The ***Core Module*** estimates the geolocation shifts between MROI and high-resolution reference data in the NIR and TIR spectra by using features which are clearly identifiable in MROI data sets such as lakes, islands and coastline segments. The Reporting and Analysis Module handles the visualisation, evaluation and analysis of geolocation shifts estimates and generation of reports. Figure 1 shows the concept of the processing line. Input to the procedure are Level1B (swath geometry) MROI data from METOP AVHRR/3, and Sentinel-3A/B SLSTR and OLCI. The modular design allows for the addition of upcoming MROI sensors, potential candidates are discussed in section 5.3.

During the import of the MROI data several tests are performed to check if the selected MROI data window is suitable for matching. The MROI data window is checked for poor illumination conditions (such as polar night), which is critical for VIS, NIR and SWIR bands. If this test is passed, then checks for cloud and snow coverage are performed, applying multispectral classification using several spectral bands of the MROI sensor to be processed [RD-1]. The classification rules are optimized based on the spectral capabilities of the different sensors. Data windows affected by polar night, cloud or snow cover are not used geo-location analysis and are flagged in the Geo-location Assessment Database.

Cloud free MROI data windows are used for assessment of the geo-location accuracy relative to the reference data sets. For each matching result statistical parameters are estimated to grade the matching quality. The result of the matching module is stored in the Geo-location Accuracy Database for each GCP, together with matching quality parameters and metadata information.

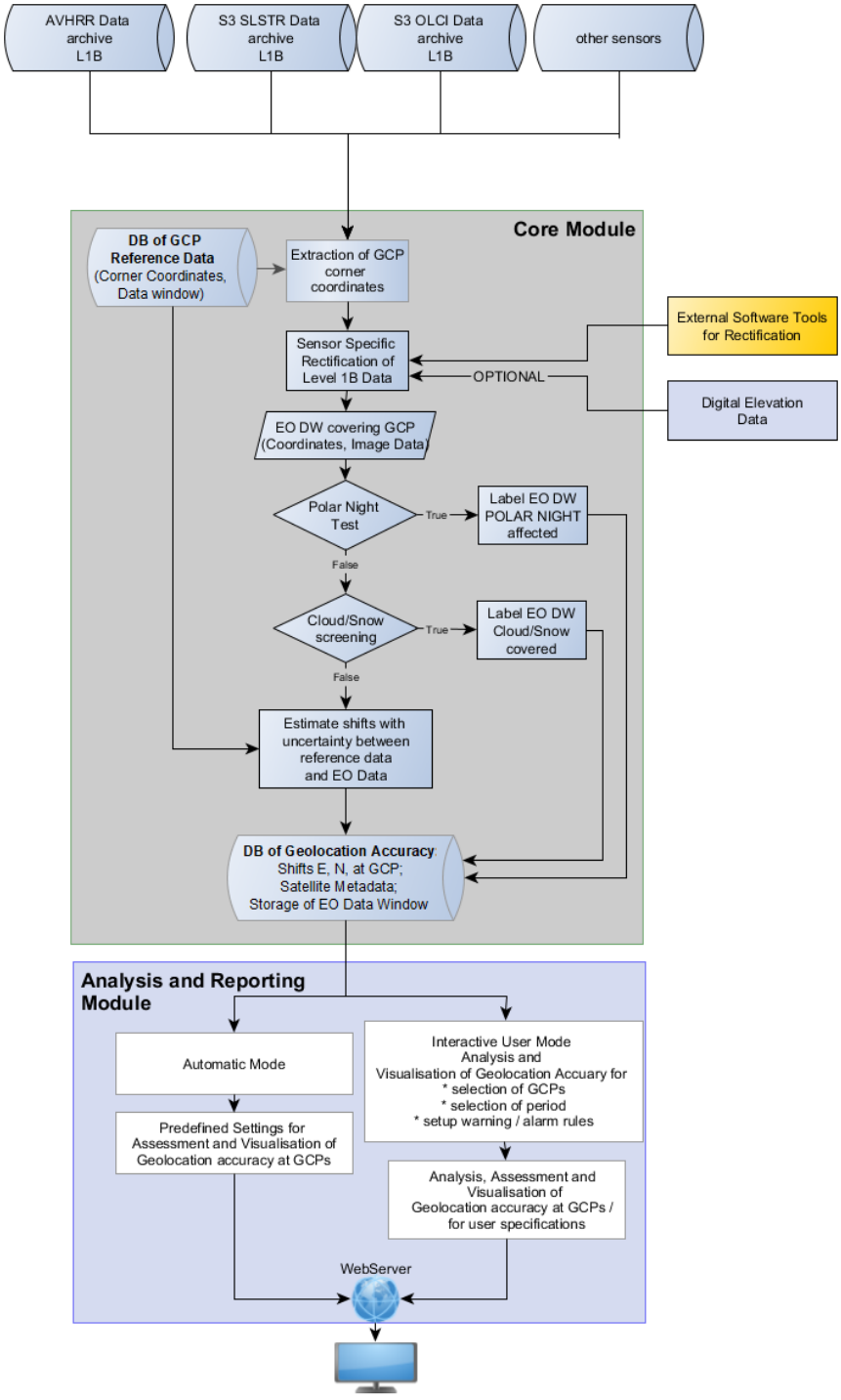

Figure 1 System concept for geolocation assessment and reporting.

The ***Reporting and Analysis Module*** is independent from the Core Module and enables the analysis and visualisation of geo-location results for selected sensors. It uses the matching result stored in the Geo-location Accuracy Database. The reporting module will run in two modes, (i) an automatic reporting mode, and (ii) in a user interactive mode for visualizing and analysing of geolocation results. The reporting module supports trend analysis, outlier removal and selection of groups of reference targets, and allows for setting alarms/warnings. As well as password protected user access to store analysis preferences for the report generation.

3. EVALUATION OF TESTED MATCHING METHODS

In general, two image matching methods exist which are summarized in [RD-4]. The area-based matching determines the similarity of the image grey level values via cross-correlation. The feature-based technique matches unique and features like edges, corners or points. In literature both methods are applied to assess the geolocation accuracy [RD-4].

During the project different matching methods and edge detection algorithms were investigated. This section summarizes the findings and considerations. It provides the rational for the implemented iterative approach of the area-based cross-correlation method which is applied to the NIR and TIR bands of the MROI-DataWindows (MROI-DW).

3.1. Cross-Correlation (Phase Correlation)

To ensure reliable shifts the matching algorithm is applied to cloud free MROI-DWs (NIR and TIR bands). For daytime acquisition cloud masks provided in the MROI product or the spectral information is used to exclude cloud and snow covered MROI-DW [RD-1].

In this project the efficient subpixel image registration algorithm proposed by [RD-3] was selected. The algorithm is available in Python's scikit-image library [RD-7]. It calculates the normalized cross-correlation matrix using the Discrete Fourier Transforms of the input DW, which is a standard method in image and signal processing. The location of the maximum value in the correlation matrix relative to the centre of the correlation matrix (corresponding to no shift) is derived which corresponds to the shift in terms of pixels

Sub-pixel accuracy is achieved by oversampling of the cross-correlation matrix using the single-step DFT (Discrete Fourier Transform) approach described in detail in [RD-1]. This method for estimating the sub-pixel shift has the advantage that it accounts for peaks in the correlation matrix with asymmetric shape [RD-1].

Reliable shift estimation for TIR bands is in general not possible during the night without any additional cloud information. Furthermore, the thermal signature of the imaged MROI-DW might differ from the signature depicted in the GCP-DW. Thermal signatures of observed land features show a seasonal and diurnal dependence resulting in erroneous shift estimates if matched against any reference image with opposing thermal signatures.

Edge detection algorithms were applied to the resampled MROI-DW to overcome the aforementioned limitations. The tested methods comprise of the i) Sobel-Operator, ii) Laplace Operator and iii) Local Entropy. After the edge detection, the image with the enhanced edges was matched using the cross-correlation against an edge enhanced reference image. In addition, the method of mutual information was tested for image registration. These techniques are described below.

3.2. Sobel-Operator

The Sobel-Operator is a standard method in image processing to enhance and detect edges in an image. It computes an approximation of the image gradient in vertical and horizontal direction within a 3x3 filter kernel. Emphasized edges might contain incorrectly classified edges or can exhibit broken

lines. Before applying the Sobel-Operator noise within the image is reduced to avoid identification of pixels that do not belong to an edge. The top panel in Figure 2 illustrates the principle of the edge detection. The grey value ($g_{(x)}$) distribution along a profile transitions from low values over the water (left) to high intensity area over land (right). The pronounced peak in the second panel corresponds to this edge detected by the Sobel-Operator.

Enhanced edges of the Landsat-8 and SLSTR are presented in the second column of Figure 3 (NIR bands) and Figure 4 (TIR bands). The Sobel-Operator is applied to images in their native resolution. The contrast between water bodies and surrounding land mass is enhanced. However, areas with small grey value variations remain (Figure 3). If the discontinuities in the image are less pronounce as depicted in Figure 4 (SLSTR S8_in, daytime), then no edges are found or pixels are classified incorrectly (Figure 4 SLSTR S8_in, cloud north east of Lake Garda, night-time).

3.3. Laplace Operator

The Laplace-Operator searches for zero crossings in the second derivative within a 3x3 filter window. This conveniently highlights grey level discontinuities caused by edges. Areas with slowly varying grey levels are dampened. This operation produces highlighted edges and other discontinuities against a dark background. Emphasized edges (e.g. at clouds, etc) might contain incorrectly classified edges or can exhibit broken lines; this can be solved by applying filtering where needed. The lower panel in Figure 2 presents the 2nd derivative of the edge show in the top panel.

The results of the Laplace-Operator applied to the Landsat-8 and SLSTR are presented in the third column of Figure 3 (NIR bands) and Figure 4 (TIR bands). The homogenous area of the lake is clearly identified, but the noise on the land is enhanced andis undesirable. In addition, contrast enhancement to redistribute pixel values and equalize the histogram would be required.

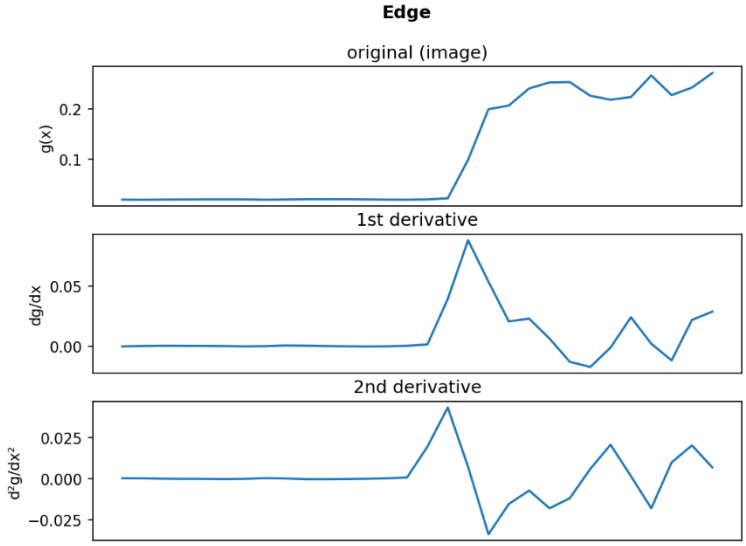

Figure 2 Qualitative plot of a profile through the grey values g(x) of an edge and its derivatives. Left half reflects the low values of a water body, higher values in the right half correspond to land surfaces.

3.4. Local Entropy

Within a defined neighbourhood (e.g.: 5-by-5) the image entropy is computed and assigned to the central pixel of the filter window. It is a statistical measure of randomness of the images grey values

and it can be used to enhance edges of the input image. Areas with similar grey values in the input image result in homogenous areas in the entropy image. Transitions zones as the difference between water and land are highlighted. A cloud free MROI-DW even acquired at a different season or daytime shows the same image patterns as the reference image. However, this method is sensitive to the size of the filter window and the resolution of the MROI. This could lead to blurred shorelines and artefacts along pixel boundaries (last column in Figure 3 and Figure 4).

In general, gradient operators emphasize noise in the image as well. Therefore, noise removal has been proven beneficial before applying such operators Identified edges can exhibit breaks which require linking the segments to close these gaps. For remaining pixels that are not part of an edge need to be eliminated.

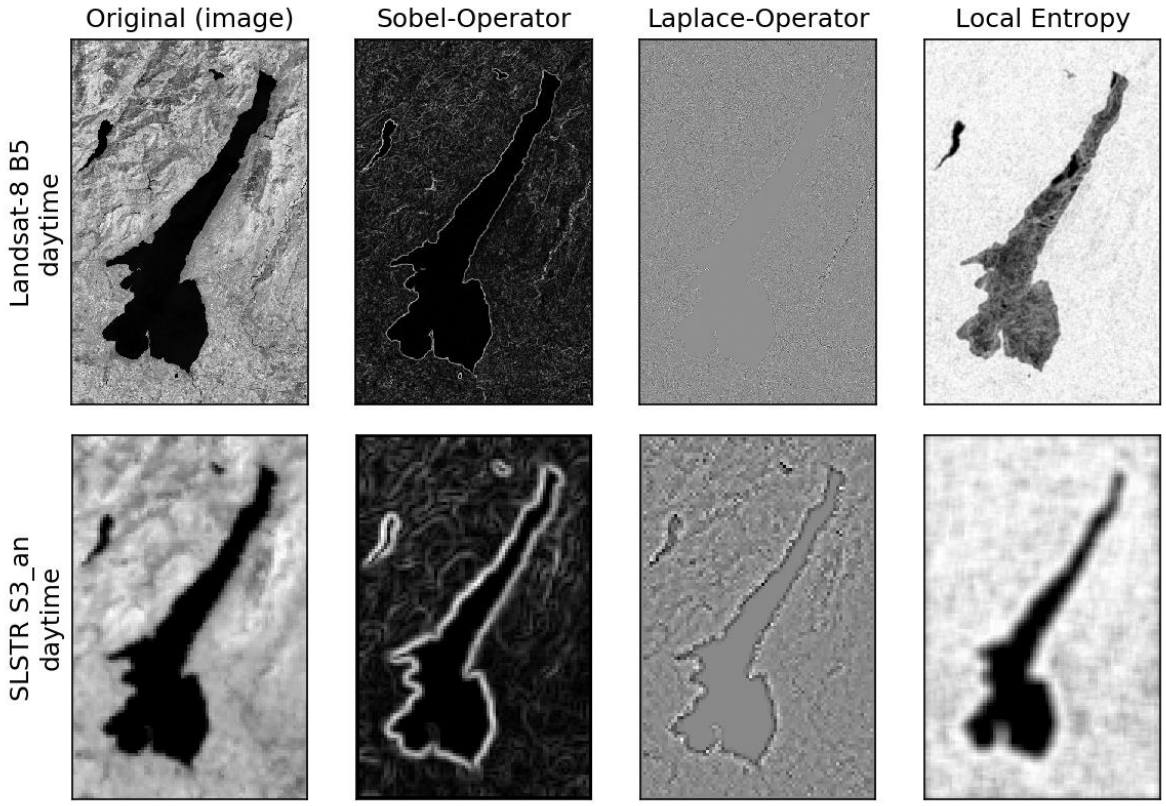

Figure 3 Edge detection algorithms applied to NIR band B5 of Landsat-8, LC08_L1TP_193028_20160717_20170323_01_T1 (top row) and NIR band S3_an of SLSTR, S3A_SL_1_RBT____20170706T093528_20170706T093828_20181004T170037_0179_019_307_____LR1_R_NT_003.SEN3) both scenes where acquired during the day.

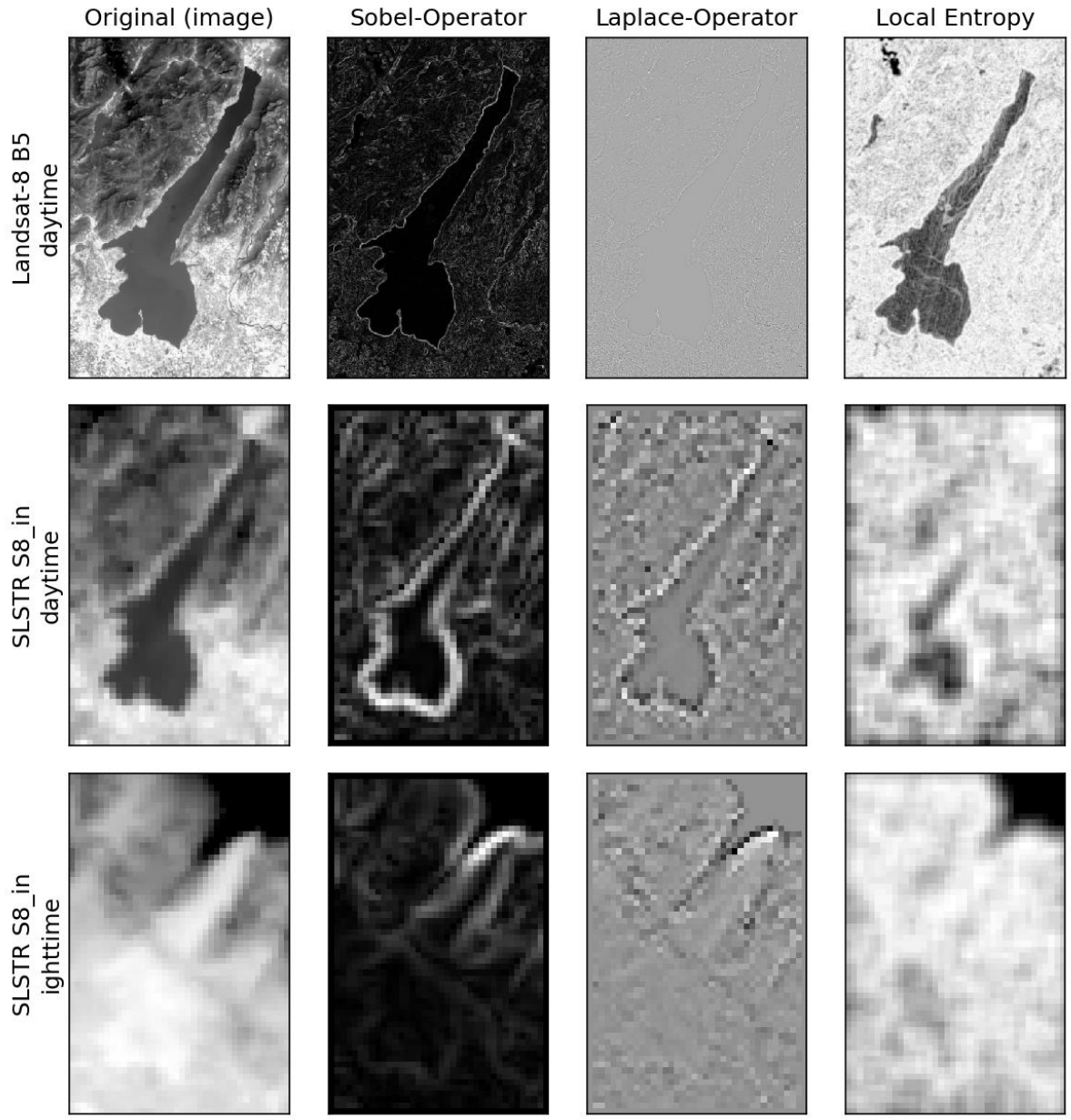

Figure 4 Edge detection algorithms applied to TIR band B10 of Landsat-8, LC08_L1TP_193028_20160717_20170323_01_T1 (top row) and TIR band S8_in of SLSTR, S3A_SL_1_RBT____20170706T093528_20170706T093828_20181004T170037_0179_019_307_____LR1_R_NT_003.SEN3) both scenes where acquired during the day. Bottom row shows TIR band S8_in of SLSTR, S3A_SL_1_RBT____20170706T205823_20170706T210123_20181004T171402_0179_019_314_____LR1_R_NT_003.SEN3) acquired at night

3.5. Mutual Information

Mutual information (MI) is a measure from information theory which quantifies the mutual dependence between the two variables. MI is extensively utilized in medical imaging to align images which are acquired by different techniques. The basic assumption in medical imaging is that regions of similar tissue (and hence similar grey values) in one image correspond to regions in the other image that also consist of similar grey values [RD-6]. The constructed feature space, a joint 2D histogram, provides the combinations of grey values in each of the two images for all corresponding points. The second image is shifted until the mutual information between it and the reference image is maximized.

In the context of this project this assumption only holds for cloud free scene. MI would account for different thermal signatures in the GCP-DW and MROI-DW. This allows MI to match scenes acquired in different seasons and hence with different thermal signatures. On the other hand, this method is computationally expensive, and images are registered not on sub-pixel level. This means that for cloud free scenes (daytime) the cross-correlation method brings the same result at a lower computational cost. To match scenes collected during different seasons it would be beneficial to extend the existing reference dataset to cover typical thermal signatures of each season. (see chapter 5)

3.6. Iterative approach (Cross-Correlation)

To reach sub-pixel accuracy in the matching process the phase correlation is applied in an iterative manner. Each MROI-DW consist of one data array and one geolocation grid with the geographic location of each pixel in the data array. After the resampling [RD-1] the GCP-DW and the MROI-DW are matched against each other with the phase correlation method readily available in the scikit-image library [RD-7]. This shift estimate is added component wise to the geolocation grid to account for the misregistration. Intermediate quality measures such as the Signal-to-Noise Ratio (SNR) and the correlation coefficient are stored temporarily and used to quantify the quality of the shift estimate. This process is repeated until the shift estimate converges below a customizable threshold or a specified exit criterion is met [RD-1].

3.7. Conclusion Matching methods

For this project it was decided to use a computationally efficient phase correlation method. In addition to the implemented oversampling of the cross-correlation matrix, a parabolic interpolation method was introduced to reach sub pixel level.

No edge detection was implemented because of the necessary pre-processing steps, such as noise removal and the dependence on the result on the size of the filter element. These additional processing steps may introduce uncertainties to the shift estimates, especially on already unfavourable image condition like different seasons or night acquisitions.

Thermal bands collected during the night are matched without any snow/ cloud screening or pre-processing since no spectral information is available. The correlation coefficient and the SNR are used as quality measures.

4. EXAMPLES OF MATCHING RESULTS OF IMPLEMENTED METHOD

This section provides an overview and a discussion on the matching results derived with the OSMON software package. The plots depicted in this section were directly exported form the OSMON Webtool. Red lines in the time series indicate the 7-day moving average and reddish band indicates ± 1 standard deviation. The abscissa provides the shift in true meters positive towards East (ΔE_{true}) and on the ordinate the shift in true meters (ΔN_{true}) is positive towards the North. Each individual shift estimate is represented by a dot. All analysed data sets were acquired in 2017 during daytime .

4.1. AVHRR3

The Advanced Very High-Resolution Radiometer 3 (AVHRR3) operates onboard of MetOP -A and-B satellites. AVHRR3 is a multi-purpose imaging instrument used for global monitoring of cloud cover, sea surface temperature, ice, snow and vegetation cover characteristics. AVHRR3 is an across-track scanner that senses the Earth's outgoing radiation from horizon to horizon in six channels (4 VIS/NIR bands, 3 of them will be transmitted, and 2 TIR bands), with a spatial resolution of about 1.1km at nadir. AVHRR3 products provide geolocation for tie points along the scan line, as well as their satellite and solar zenith and azimuth angles. Tie point geolocation is estimated with a satellite ephemeris model and an instrument scanning model. In this section shift estimates for AVHRR3 of MetOP-B are discussed.

4.1.1. Shift estimates (NIR, CH2)

The analysis of one year (01.01.2017 to 31.12.2017) of AVHRR3 (MetOP- B) data is summarized in Table 1. An average shift of 1361m Westwar (Figure 5) and 121 m Southward (Figure 6) can be expected for the NIR channel CH2.

Table 1 Statistics for one year (01.01.2017 to 31.12.2017) of AVHRR3 (MetOP- B) data. Number of calculated shifts is 3455.

	ΔE_{true} [m]	ΔN_{true} [m]
mean	-1361	-121
rms	1033	624
std	1033	624
median	-1077	-168
68%	-824	21
90%	-471	461
95%	-296	890

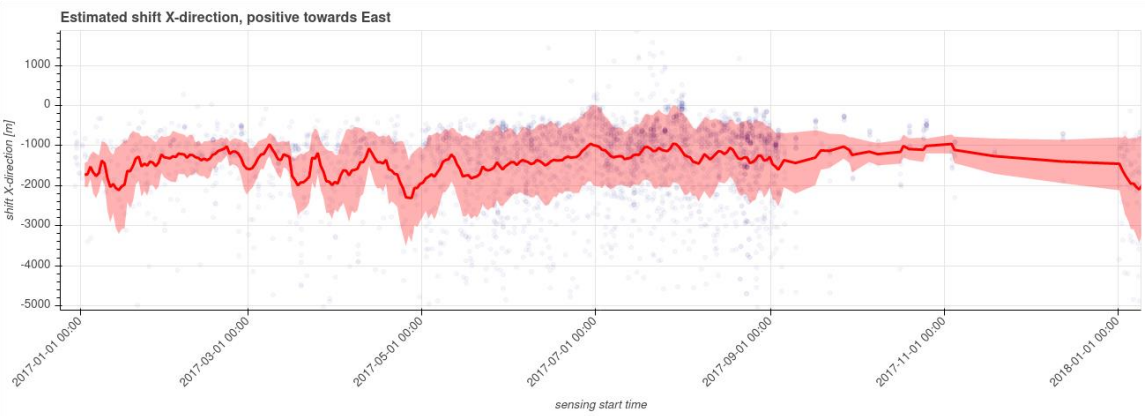

Figure 5 Timeseries of shift estimates in X direction (positive towards East) of one year (01.01.2017 to 31.12.2017) of AVHRR3 (MetOP-A and B) channel CH2 data. Number of calculated shifts is 3455.

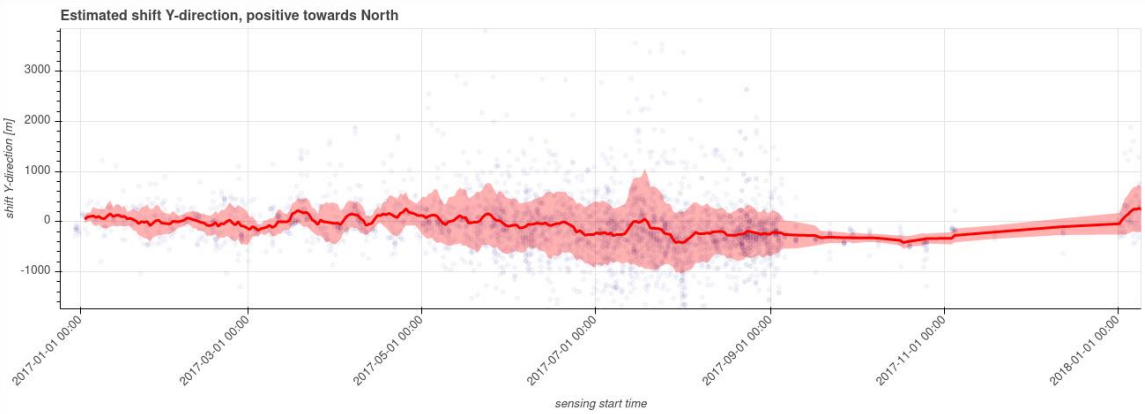

Figure 6 Timeseries of shift estimates in Y direction (positive towards North) of one year (01.01.2017 to 31.12.2017) of AVHRR3 (MetOP-A and B) channel CH2 data. Number of calculated shifts is 3455.

AVHRR3 data is georeferenced and therefore the position of the GCP within the swath is critical. The spacing of the geolocation grid increases from roughly 1100 m at nadir towards the swath boundaries. This effect is clearly visible in Figure 7 and Figure 8. For view elevation angles below 60°, the spread in the shift estimates is up to ±4000 m. Observations close to nadir (view elevation angles of 90°) reveal smaller variation in the shift estimates.

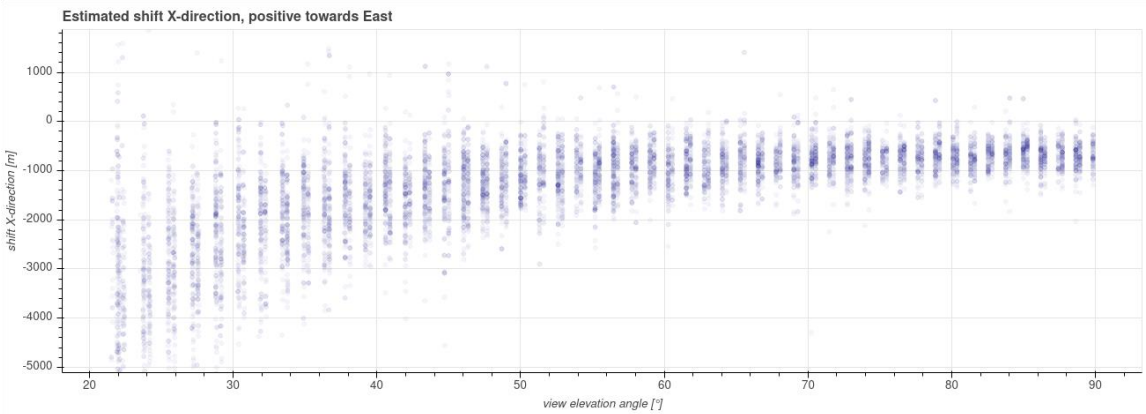

Figure 7 Shift estimates (CH2) of ΔE_{true} [m] in dependence of the view elevation angle (nadir corresponds to 90°). The variation decreases when the GCPs are observed close to nadir.

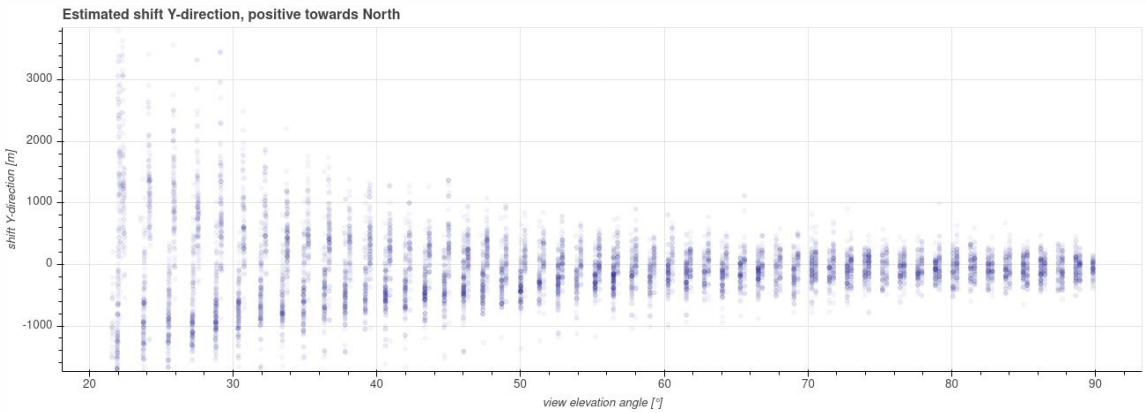

Figure 8 Shift estimates (CH2) of ΔN_{true} [m] in dependence of the view elevation angle (nadir corresponds to 90°). The variation decreases when the GCPs are observed close to nadir.

4.1.2. Shift estimates (TIR, CH4, daytime acquisitions)

The mean shift estimates in North-South direction of -114 m for the thermal channel CH4 (MetOP-B) is within the same order of magnitude as the NIR channel CH2. In East-West direction, the shift is -1805 m, which is nearly twice the estimated shift compared to the NIR band.

Table 2 Statistics for one year (01.01.2017 to 31.12.2017) of AVHRR3 (MetOP- B) channel CH4 data. Number of calculated shifts is 1588.

	ΔE_{true} [m]	**ΔN_{true} [m]**
mean	-1805	-114
rms	1203	928
std	1204	928
median	-1465	-232
68%	-1172	-27
90%	-814	656
95%	-610	1538

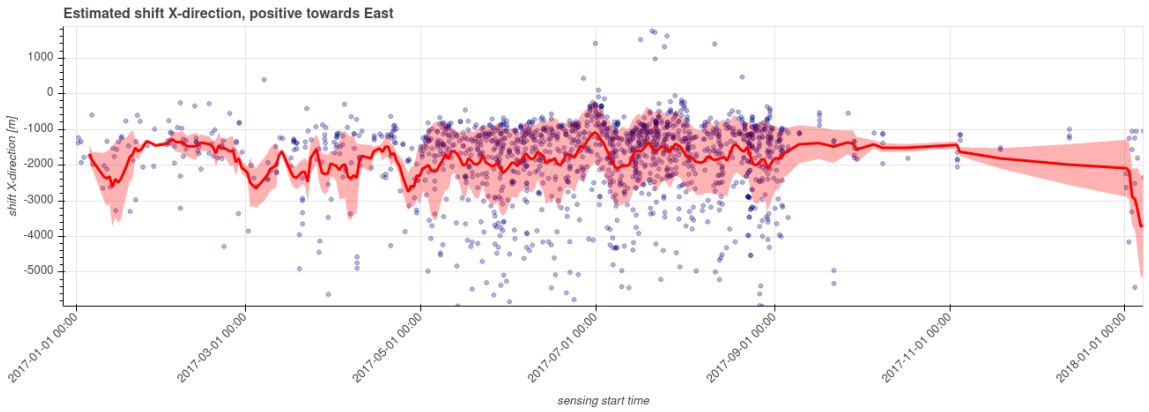

Figure 9 Timeseries of shift estimates in X direction (ΔE_{true} [m] positive towards the East) of one year (01.01.2017 to 31.12.2017) of AVHRR3 (MetOP-B) channel CH4 data.

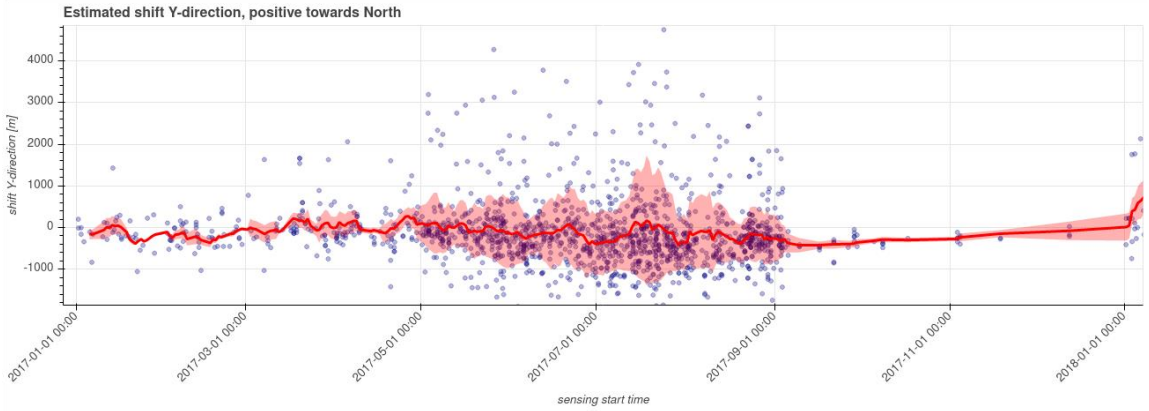

Figure 10 Timeseries of shift estimates in Y direction (ΔN_{true} [m] positive towards the North) of AVHRR3 band CH4

The reduction of the shift estimates as they approach nadir is in band CH4 also clearly visible in Figure 11 and Figure 12.

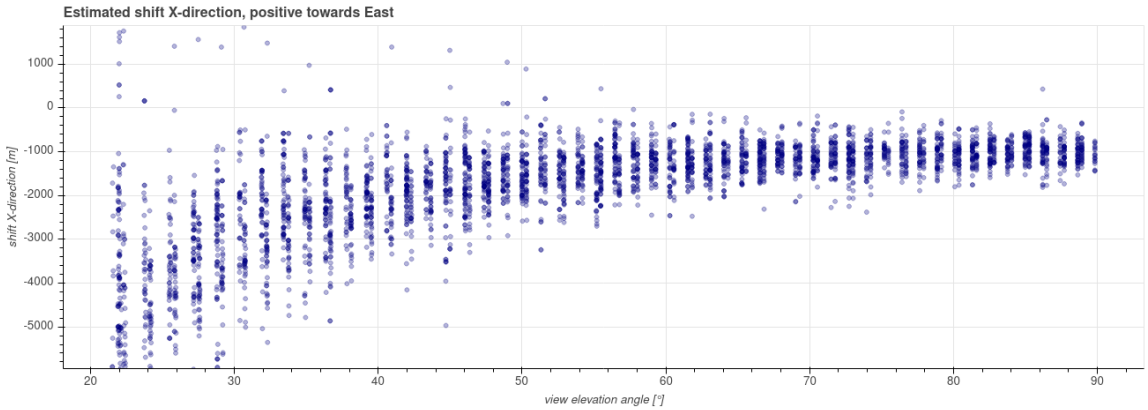

Figure 11 Shift estimates (CH4) of ΔE_{true} [m] in dependence of the view elevation angle (nadir corresponds to 90°). The variation decreases when the GCPs are observed close to nadir.

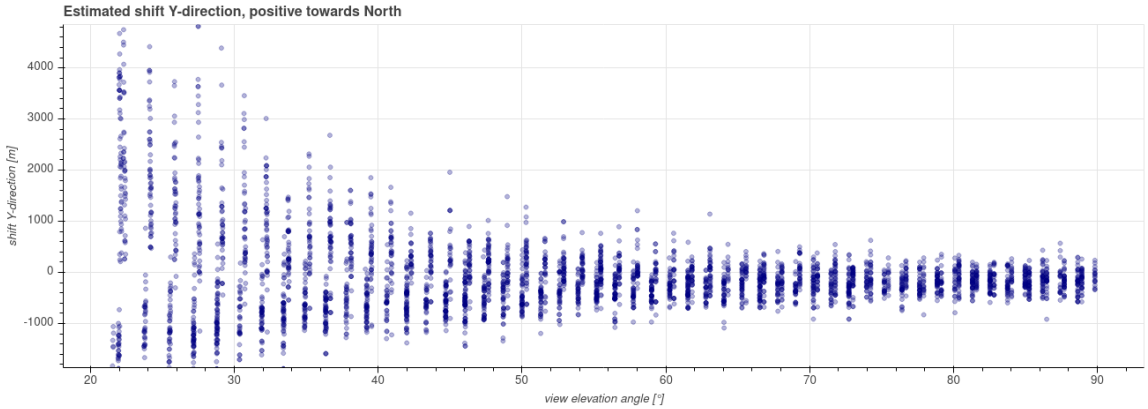

Figure 12 Shift estimates (CH2) of ΔN_{true} [m] in dependence of the view elevation angle (nadir corresponds to 90°). The variation decreases when the GCPs are observed close to nadir.

4.2. SLSTR (nadir, oblique)

The Copernicus Sentinel-3 mission consists of 2 identical satellites (A and B), both carrying two optical sensors, the Sea and Land Surface Temperature Radiometer (SLSTR), and the Ocean and Land Colour Instrument (OLCI). SLSTR is a conical scanning imaging radiometer employing the along-track scanning dual view technique. It delivers measurements at a spatial resolution of 500 m for VIS and SWIR channels and at 1 km for the TIR and FIRE channels. Level SLSTR Level-1B processing consists of measurement calibration, time domain averaging of SWIR channels, re-gridding into co-located along track and nadir images, and cosmetic filling of all missing pixels. Accurate rectification requires to go back from this image grid to the instrument grid, remove cosmetic pixels, and take accurate tie point grids during the transformation to the map projection into account.

4.2.1. Shift estimates (NIR, band S3, stripe a, view nadir)

The analysis of one-year (01.01.2017 to 31.12.2017) SLSTR (Sentinel-3A) data is summarized in Table 3. An average shift of 12 m towards the West (Figure 13) and 20 m towards the South (Figure 14) can be expected for in band S3a at nadir. The deviation from the median values is caused by the five events with larger shift estimates. Each event is limited to one day. The cause of this clearly visible events (Figure 13, arrows) in March, July, September and December is unclear. These features are not detectable in the OLCI timeseries. Therefore, the cause is likely related to the instrument or to the processing and not to the platform.

Table 3 Statistics for one year (01.01.2017 to 31.12.2017) of SLSTR (Sentinel-3A, band S3, stripe a, view nadir) data. Total number of calculated shifts is 14430

	ΔE_{true} [m]	**ΔN_{true} [m]**
mean	-12	-20
rms	189	141
std	189	141
median	-9	-4
68%	25	21
90%	95	65
95%	136	92

Figure 13 Timeseries of shift estimates in X direction (ΔE_{true} [m] positive towards East) of SLSTR band S3, stripe a, view nadir. Arrows mark days with larger shift estimates. The window of moving average is set to 7 days which blurs the single day event over one week.

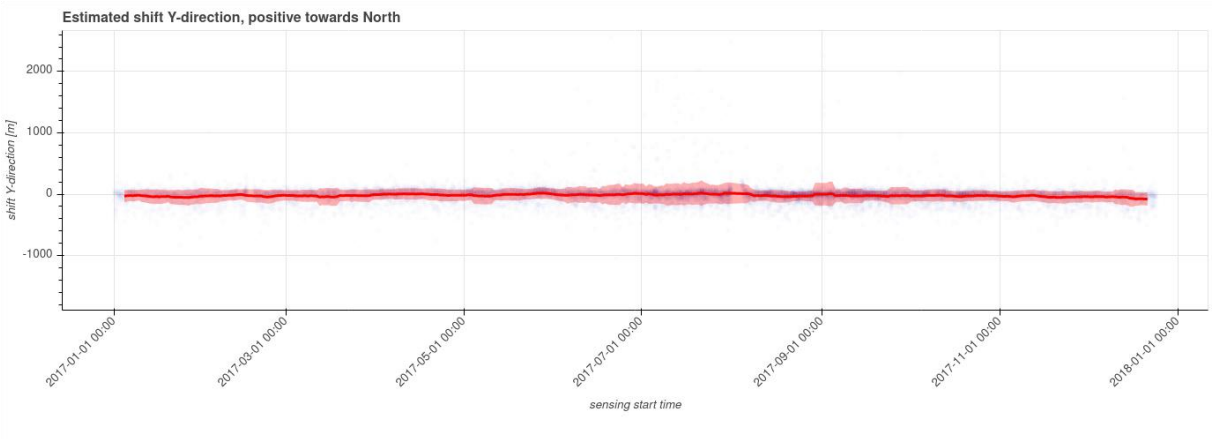

Figure 14 Timeseries of shift estimates in Y direction (ΔN_{true} [m] positive towards North) of SLSTR band S3, stripe a, view nadir

SLSTR products are ortho-geolocated, that is, the geodetic position is corrected for the real altitude of the Earth's surface. This eliminates the dependence of the shift estimate on the view elevation angle compared to AVHRR3 (section 4.1). However, for MROI-DWs observed below a view elevation angle of 50° the variation is still larger than compared to nadir observations in both directions (Figure 16 and Figure 15).

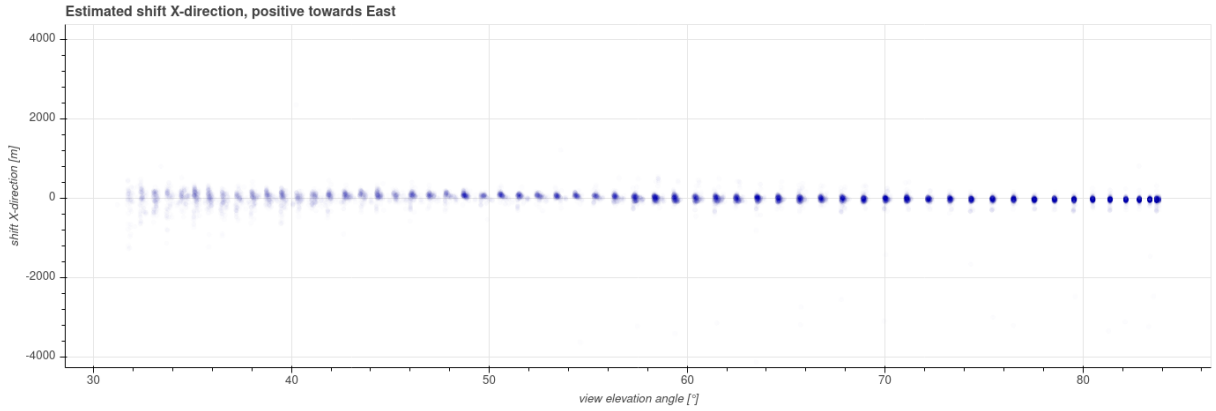

Figure 15 Shift estimates (SLSTR band S3, stripe a, view nadir) of ΔE_{true} [m] in dependence of the view elevation angle (nadir corresponds to 90°). The variation decreases when the GCPs are observed close to nadir.

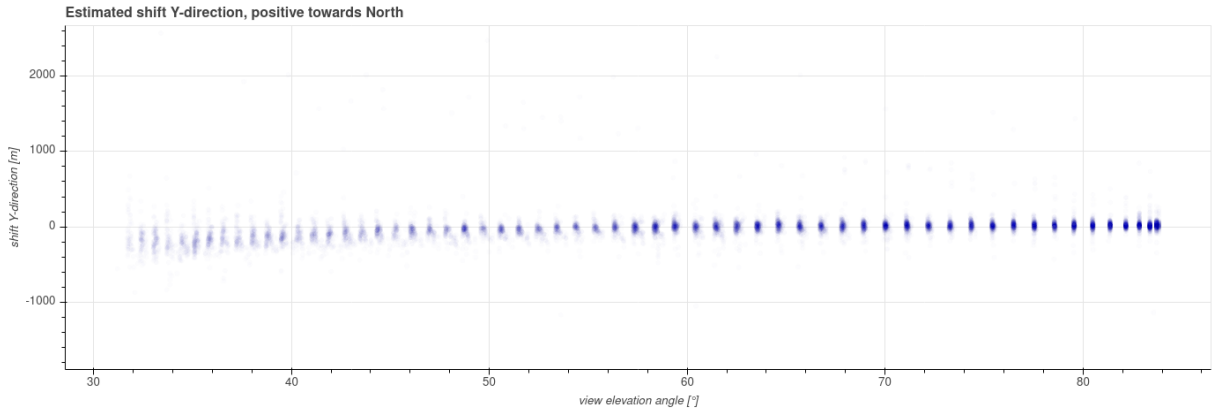

Figure 16 Shift estimates (SLSTR band S3, stripe a, view nadir) of ΔN_{true} [m] in dependence of the view elevation angle (nadir corresponds to 90°). The variation decreases when the GCPs are observed close to nadir.

4.2.2. Shift estimates (NIR, band S3, stripe a, view oblique)

Due the instrument geometry, the view elevation angle in the oblique view is fixed to ~35°. This ultimately results in larger shift estimates (Table 4). The depicted shift estimates were computed for one year (01.01.2017 to 31.12.2017) of SLSTR (Sentinel-3A, band S3, stripe a, view oblique) data. The number of calculated shifts (6252) is smaller compared to the nadir direction (14403), because of the smaller footprint in oblique acquisition. Caused by the salting imaging geometry, the shift estimates are on average shifted by 15 m towards the East and 162 m towards the South. Especially the shift estimate in ΔN_{true} is by a factor of 8 larger. The features with larger shifts, which were found in figure 4.2.1, are also visible observable in the oblique dataset. The cause of this clearly visible one day lasting events (Figure 13 arrows) in March, July, September and December is unclear. These features are not detectable in the OLCI timeseries nor in the timeseries of the thermal band S8. Therefore, it was concluded that the cause is related to the processing of the NIR bands.

Table 4 Statistics for one year (01.01.2017 to 31.12.2017) of SLSTR (Sentinel-3A, band S3, stripe a, view oblique) data. Total number of calculated shifts is 6252

	ΔE_{true}	ΔN_{true} [m]
mean	15	-162
rms	280	245
std	280	245
median	24	-190
68%	96	-128
90%	169	-9
95%	205	88

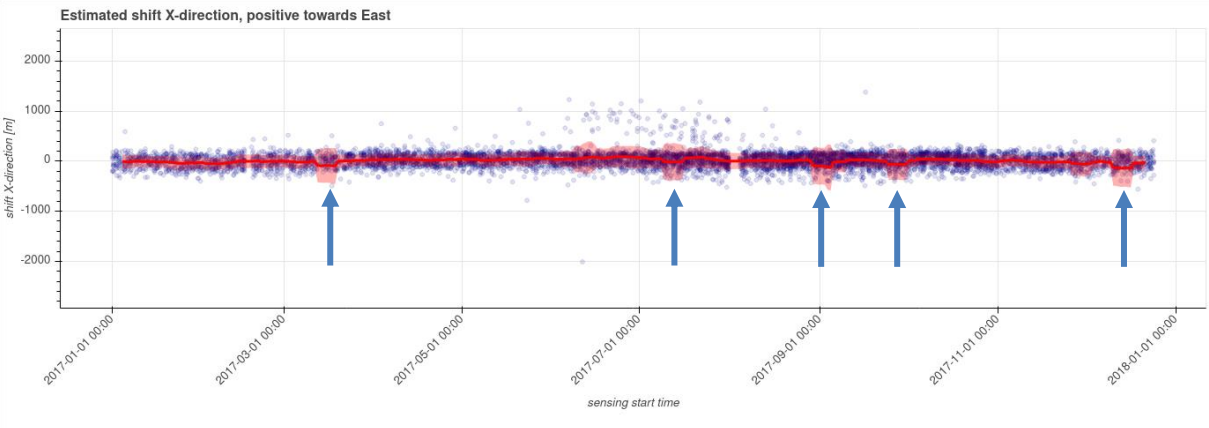

Figure 17 Timeseries of shift estimates in X direction (ΔE_{true} [m] positive towards East) of SLSTR band S3, stripe a, view oblique. Arrows mark days with larger shift estimates. The window of moving average is set to 7 days which blurs the single day event over one week.

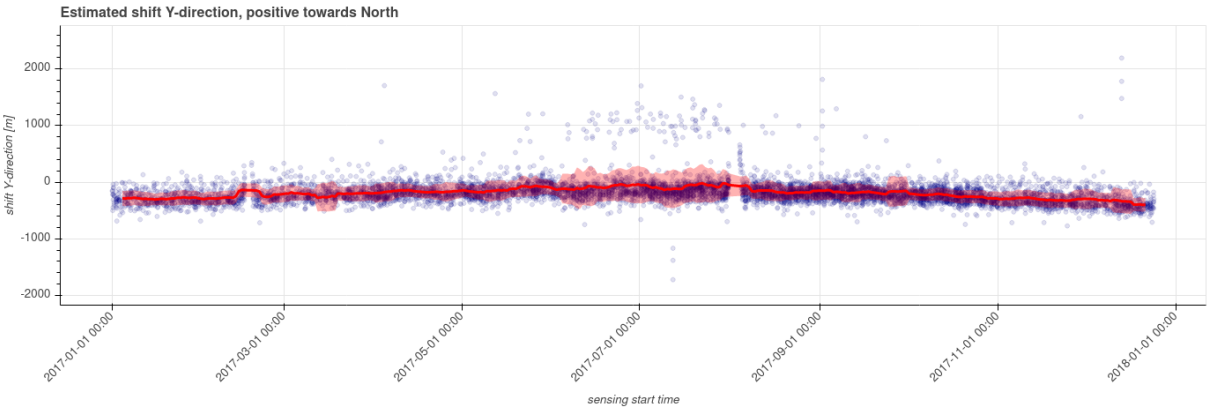

Figure 18 Timeseries of shift estimates in Y direction (ΔN_{true} [m] positive towards North) of SLSTR band S3, stripe a, view oblique

4.2.3. Shift estimates (TIR, band S8, stripe i, view nadir, oblique)

For the same time span and the same parent products the number of matching results (Table 5) of the thermal bands (7733) is roughly half the number computed in the S3_an (14430). This can be explained by the global distribution of the GCP and the assumption that acquisitions over one hemisphere have unfavourable combinations of images. In other words, half the MROI-DWs show a contrasting thermal

signature due to the season. Section 5 proposes to extend the reference dataset to cover the characteristic thermal signatures of a GCP throughout the year. The number of valid matching results is further reduced for the oblique collections due to its smaller footprint (Table 6). No trends or anomalies were observed in the timeseries of the thermal band S8_in (Figure 19 and Figure 20).

Table 5 Statistics for one year (01.01.2017 to 31.12.2017) of SLSTR (Sentinel-3A, band S3, stripe i, view nadir) data. Total number of calculated shifts is 7775

	ΔE_{true} [m]	ΔN_{true} [m]
mean	224	-150
rms	294	251
std	294	251
median	230	-115
68%	291	-59
90%	439	51
95%	530	132

Table 6 Statistics for one year (01.01.2017 to 31.12.2017) of SLSTR (Sentinel-3A, band S8, stripe i, view oblique) data. Number of calculated shifts is 3857

	ΔE_{true} [m]	ΔN_{true} [m]
mean	-71	-144
rms	416	376
std	416	376
median	-53	-161
68%	40	-45
90%	227	228
95%	354	422

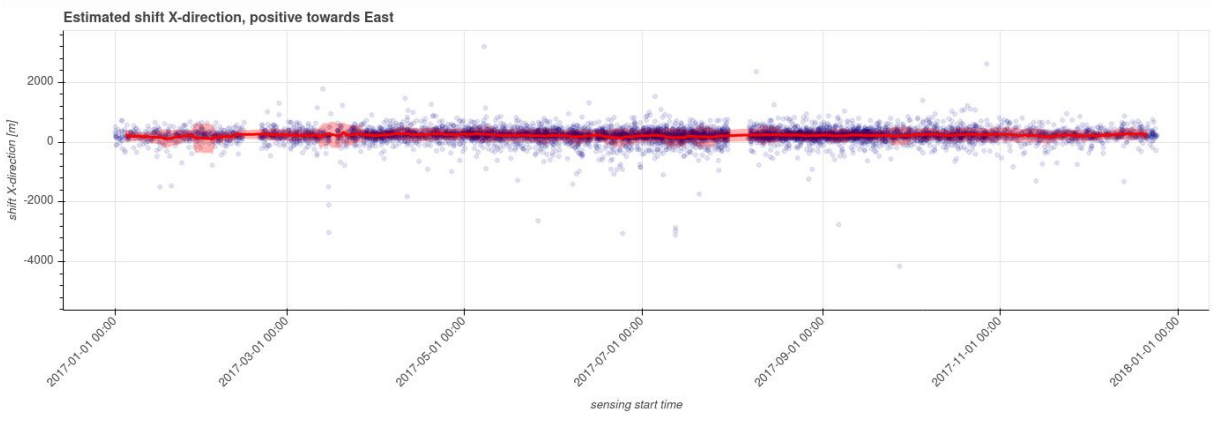

Figure 19 Timeseries of shift estimates in X direction (ΔE_{true} [m] positive towards East) of SLSTR band S8, stripe i, view nadir.

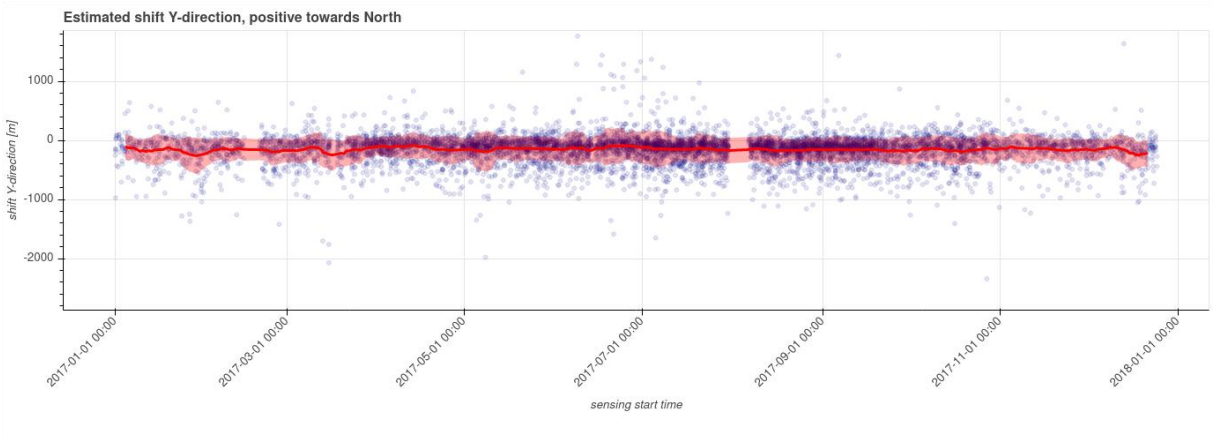

Figure 20 Timeseries of shift estimates in Y direction (ΔN_{true} [m] positive towards North) of SLSTR band S8, stripe i, view nadir.

4.3. OLCI

OLCI is a push-broom imaging spectrometer with five cameras, featuring 21 distinct bands in the 0.4-1.02 µm spectral region at 300 m spatial sampling and a swath width of 1270 km. The swath is not centred at nadir view but shifted across track by 12.6° away from the sun to minimize the impact of sun glint.

4.3.1. Shift estimates (NIR, Oa17)

The analysis of one year (01.01.2017 to 31.12.2017) of OLCI (Sentinel-3A) data is summarized in Table 7. An average shift of 53 m towards the East (Figure 21) and 98 m towards the South (Figure 22) can be expected for the NIR channel Oa17.

Table 7 Statistics for one year (01.01.2017 to 31.12.2017) of OLCI (Sentinel-3A, band Oa17) data. Total number of calculated shifts is 17622

	ΔE_{true} [m]	**ΔN_{true} [m]**
mean	53	-98
rms	171	83
std	171	83
median	65	-94
68%	90	-70
90%	132	-32
95%	153	-14

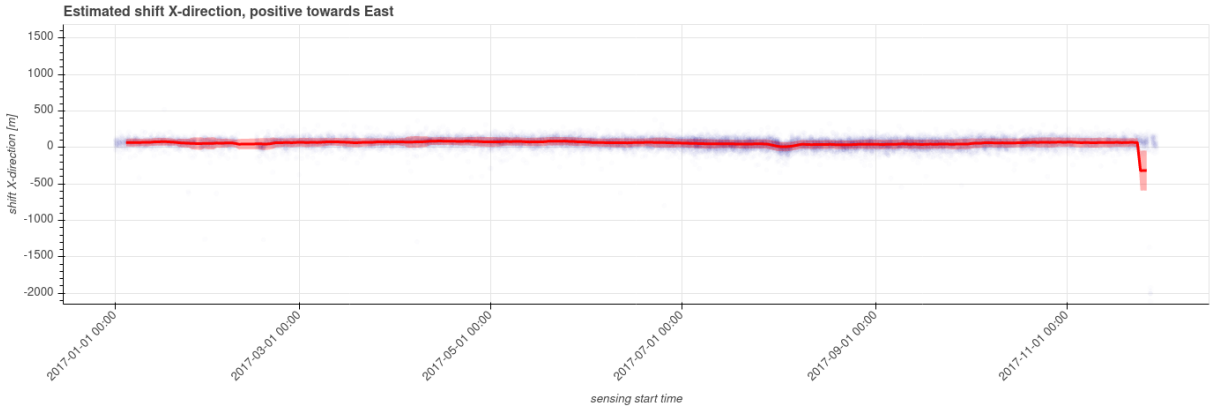

Figure 21 Timeseries of shift estimates in X direction (ΔE_{true} [m] positive towards East) of OLCI band Oa17

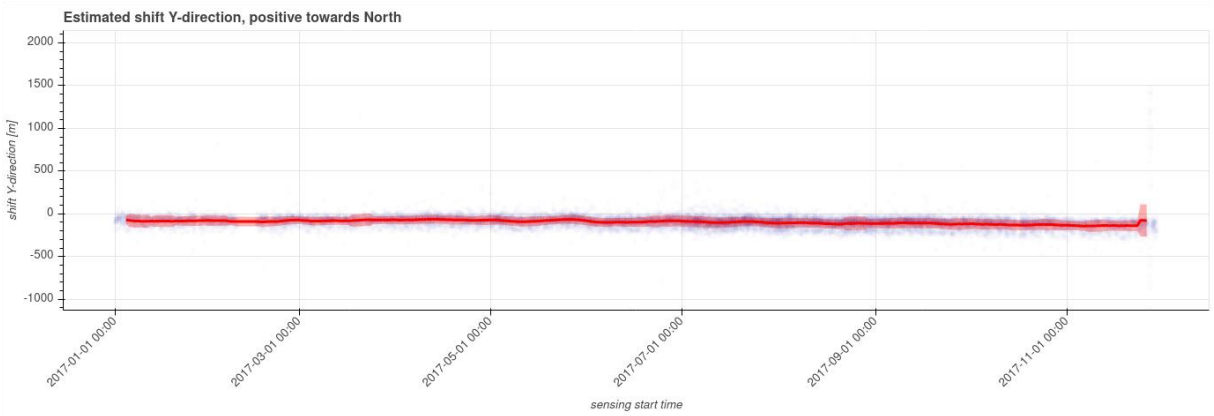

Figure 22 Timeseries of shift estimates in Y direction (ΔN_{true} [m] positive towards North) of OLCI band Oa17

OLCI products are ortho-geolocated, the geodetic position is corrected for the real altitude of the Earth's surface. The step like structure in Figure 23 is thought to be linked to the five different cameras of the OLCI instrument. The range from ~35° to ~52° would relate to camera 1, ~52° t0o ~68° to camera 2 and so forth, camera 5 maps back in the range ~68 to ~84° creating the ring like structure in Figure 24.

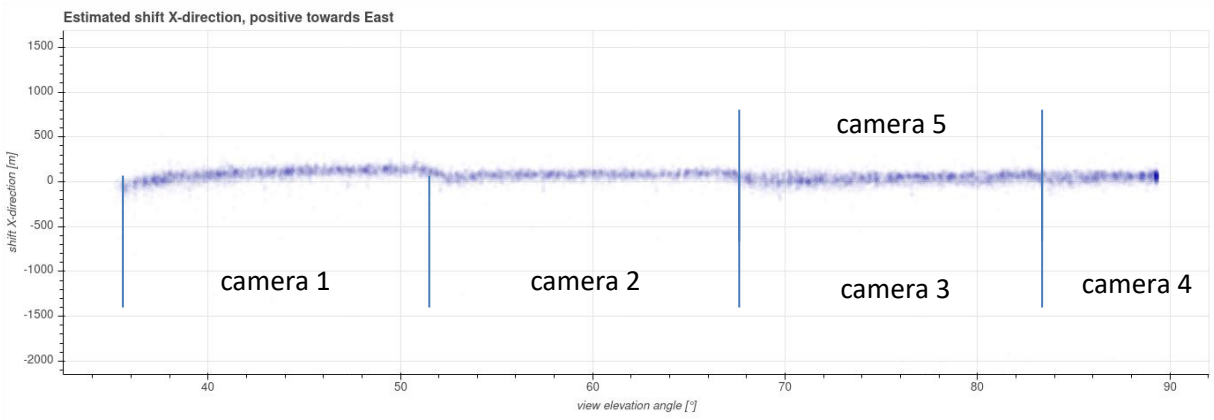

Figure 23 Shift estimates (OLCI band Oa17) of ΔE_{true} [m] in dependence of the view elevation angle (nadir corresponds to 90°). A variation of the shift estimate with the view elevation angel emerges and is linked to the 5 different cameras of the OLCI instrument.

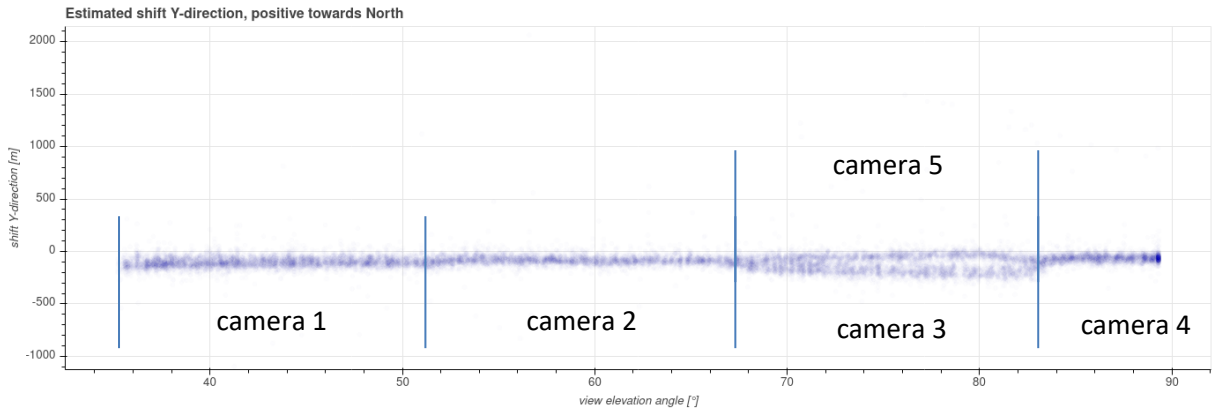

Figure 24 Shift estimates (OLCI band Oa17) of N_{true} [m] in dependence of the view elevation angle (nadir corresponds to 90°). A variation of the shift estimate with the view elevation angel emerges and is linked to the 5 different cameras of the OLCI instrument.

4.4. Conclusion Matching results

With the OSMON software an easy-to-use interface was created to evaluate and plot geolocation accuracy in dependence of various parameters like acquisition time, latitude, view elevation angle. The component-wise average shift of one year of MROI data is summarized in Table 8. It can be concluded that for e.g. AVHRR3 smaller shifts (<1/3 pixel) in North-South direction can be expected. Implying a sufficient geolocation of the scanline, but missing height information leads to incorrect positioning of the image pixel within the scanline causing higher shifts (>1/3 pixel) in East-West direction. For all other sensors, a component wise geolocation accuracy below the required 1/3 pixel [RD-8] was noted.

Table 8 Summary of one year of analysed MROI data. Shifts are provided component wise in terms of pixel

	Band	x [pix]	y [pix]
AVHRR3	CH2	-1.36	-0.12
	CH4	-1.81	-0.11
SLSTR	S3_an	-0.02	-0.04
	S3_ao	0.03	-0.32
	S8_in	0.22	-0.15
	S8_io	-0.07	0.14
OLCI	Oa17	0.18	-0.33

5. OUTLOOK FOR POTENTIAL EXTENSIONS OF OSMON

Due to the greater heat capacity of water bodies compared to land thermal signatures show a seasonal and diurnal dependence. Therefore, images collected at different seasons have varying thermal signatures. Matching thermal opposing signatures result in erroneous shift estimates and are indicated by large shift estimates and low correlation coefficients. This challenge can be addressed by extending the reference dataset with seasonal reference images as well as night reference images. Furthermore, upcoming and new sensors are an opportunity for monitoring of climate variables and

therefore it is possible to include this suite of sensors to the OSMON-software due to its modular design. In this section a way forward is sketched with potential extensions of the OSMON-software package.

5.1. Seasonal Reference Images

Wheeler Lake imaged on 10.12.2017 by MetOP-B's AVHRR3, CH4 is shifted with respect to the red GCP-Polygon (Figure 25 a/b). In panel c the thermal reference image acquired on 14.10.2015 by Landsat-8, band 10 shows good agreement with the depicted shoreline and the GCP-Polygon. However, the lake shows a lower brightness temperature than the surroundings in contrast to the AVHRR3 scene. Matching this image pair resulted in false shift estimates (x: 9099 m, y 8504 m) and a low correlation coefficient of 0.3 (Figure 25 e). On the other hand, matching the AVHRR3 scene (Figure 25 d) with a Landsat-8 scene collected in the same season (10.01.2019) with comparable thermal signature drastically improved the shift estimate to -2084 m in x and -22 m in y (Figure 25 f).

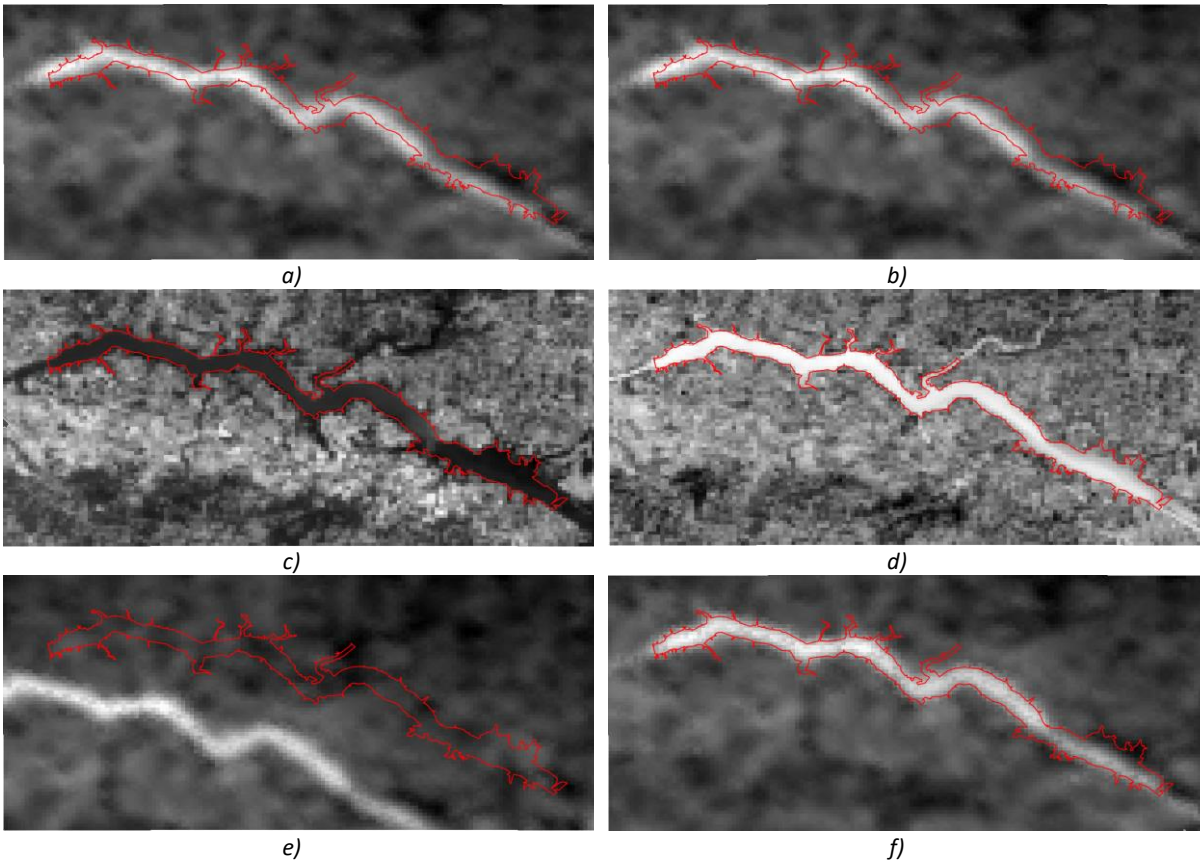

a) *b)*

c) *d)*

e) *f)*

MROI shifted by calculated shifts:

- x-shift: 9099 m
- y-shift: 8504 m
- correlation coefficient: 0.30

MROI shifted by calculated shifts:

- x-shift: -2084 m
- y-shift: -22 m
- correlation coefficient: 0.80

Figure 25 Seasonal Reference Images N034747W087264: Wheeler Lake, United States, TIR

The second example showing GCP N053421E012689: Müritzsee, Germany, TIR reveals the benefits of seasonal reference images (Figure 26). The shift estimates decreased from x: 6594 m, y: 764 m to x: 178 m and y: -428 m the correlation coefficient increases to 0.81.

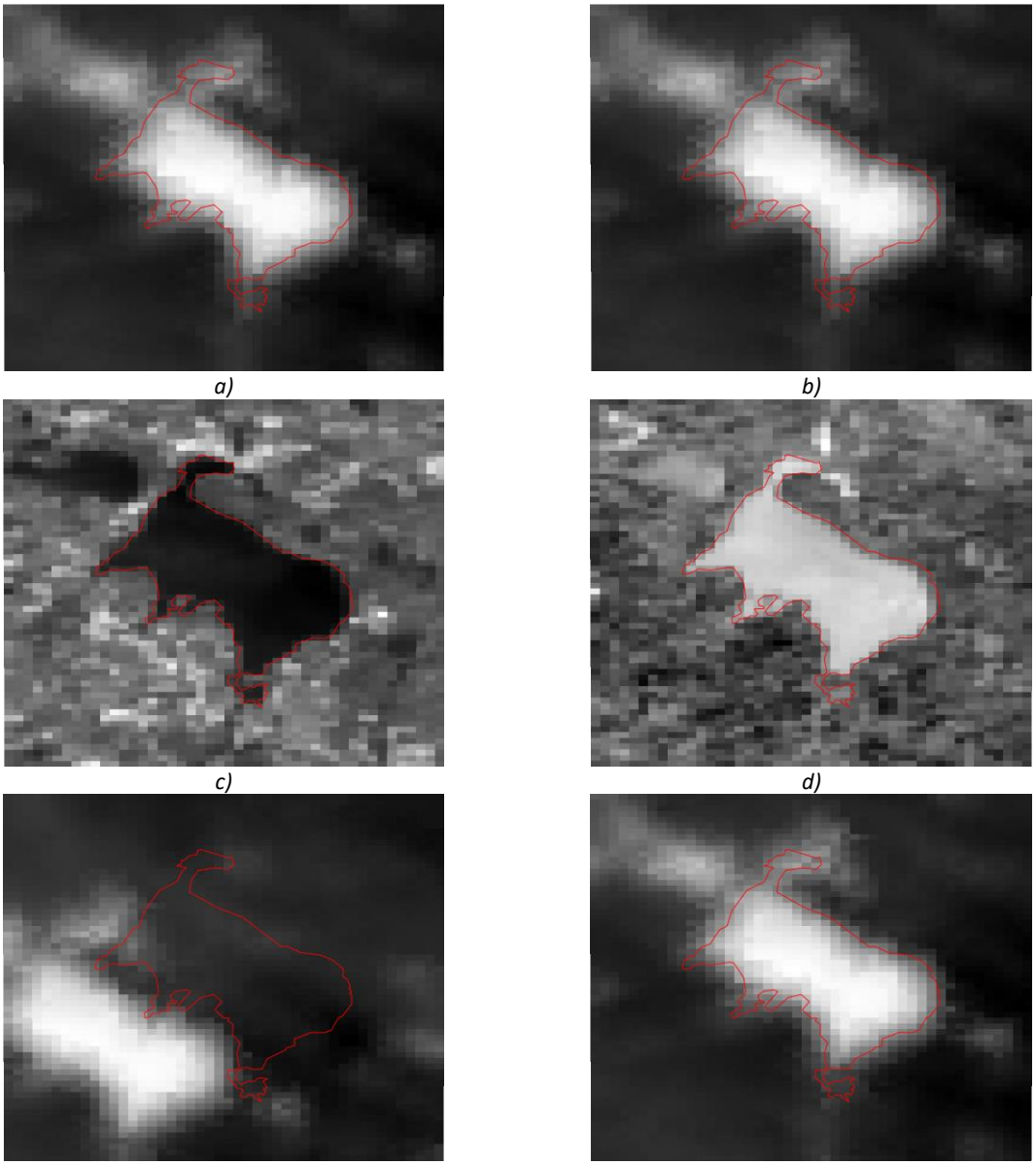

a) *b)*

c) *d)*

e) *f)*

MROI shifted by calculated shifts:

- x-shift: 6594 m
- y-shift: 5764 m
- correlation coefficient: 0.29

MROI shifted by calculated shifts:

- x-shift: 178 m
- y-shift: -428 m
- correlation coefficient: 0.81

Figure 26 Seasonal Reference Images N053421E012689: Müritzsee, Germany, TIR

5.2. Day/Night Reference Images

The principle described above occurs also on a diurnal cycle, especially in summer and autumn where strong temperature gradients between water bodies and surrounding land masses are present. For GCP N053421E012689: Müritzsee, Germany, TIR (Figure 27) a night-time acquisition was matched against a cloud free (manually selected) SLSTR night time acquisition resulting in an improved shift estimate and compared to a reference scene acquired during the day. Shifts estimates improved from x: -6689 m, y: -6981 m to x: 334 m and y: 2253 m and the correlation coefficient rose to 0.85.

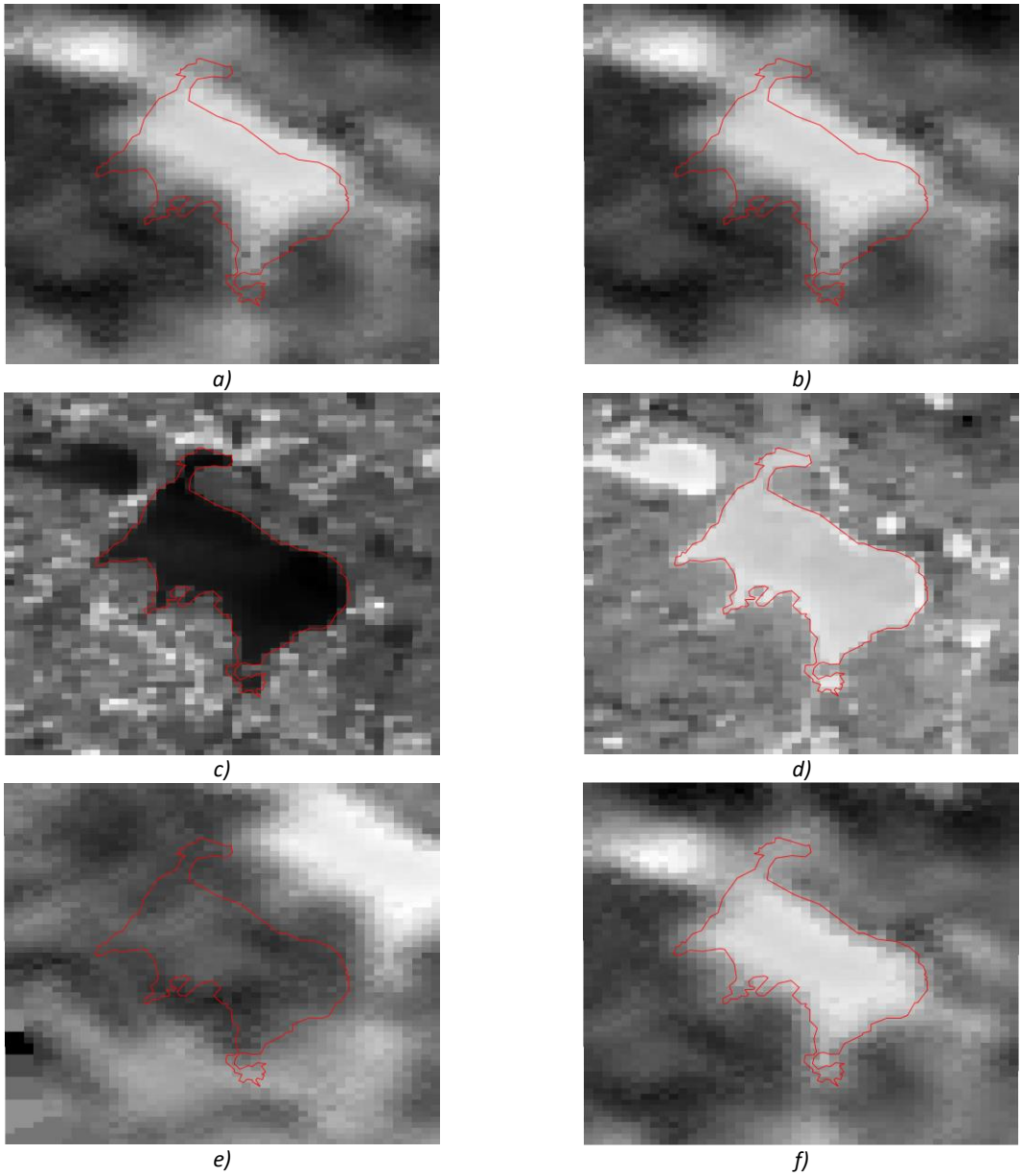

a) *b)* *c)* *d)* *e)* *f)*

MROI shifted by calculated shifts:

- x-shift: -6689 m
- y-shift: -6981 m
- correlation coefficient: 0.28

MROI shifted by calculated shifts:

- x-shift: 334 m
- y-shift: 2253 m
- correlation coefficient: 0.85

Figure 27 Day/Night Reference Images N053421E012689: Müritzsee, Germany, TIR

5.3. Implementation of new sensors

For each sensor a dedicated importer was implemented which is automatically loaded by the software. This allows to easily extent OSMON software package with new sensors. The most important prerequisite for the integration of a new sensor is that the spectral range must be captured by the high-resolution reference sensor (Sentinel-2, Landsat-8). Moreover, the dataset must have a minimum spatial extension to cover the GCPs in the Geo-location Accuracy Database. Furthermore, the metadata and its structure must be known as well as how to reflect them in the existing database tables. To load

the satellite imagery a sensor-specific importer will be developed to read the data and transform it into the implemented OSMON data and processing structure.

The OSMON reference sensor dataset can be extended for example with the upcoming Landsat 9 OLI-2/TIRS-2. Its TIRS-2 instrument overcomes the stray light issue of Landsat 8 TIRS instrument [RD-9]. An extended reference dataset refines the temporal resolution and the likelihood of cloud-free acquisitions needed for as seasonal analysis.

Table 9 Non-exhaustive list of potential reference sensors to be integrated in to OSMON

Mission	Instrument	Spectral range	Schedule
Landsat-9	OLI-2 TIRS-2	Band 5 NIR (0.85 - 0.88 µm) 30-m Band 10 TIRS 1 (10.6 - 11.19 µm) 100-m	Launch in 2021

Instruments

Earth observation missions like MetOp-SG in LEO with the METimage and 3MI instruments are potential candidates for the geolocation accuracy assessment by the OSMON tool. For these LEO missions the current version of the globally distributed GCP dataset is sufficient. Moreover, the tool is also capable of processing data from the FCI instrument onboard Meteosat Third Generation (MTG). MTG will be launched into a geostationary orbit west of Africa. Earths curvature causes distortions in the image in a radial direction extending outward from the centre of the image disk. An extension of the GCP dataset with additional African coastlines is envisioned.

Table 10 provides a non-exhaustive list of new sensors which can be integrated into the OSMON package.

Table 10 Non-exhaustive list of potential sensors to be integrated in to OSMON

Mission	Instrument	Spectral range	Schedule
MetOp-SG A	METimage	VII-17 0.865 µm VII-37 10.69 µm	Launch in 2023
MetOp-SG A	3MI	3MI-9 0.865 µm	Launch in 2023
MTG	FCI	VIS 0.8 (NIR) 0.865 µm 1.0 km IR 10.5 (TIR) 10.500 µm 2.0 km/1.0 km	Launch from 2022 onward
Sentinel-10 CHIME	Hyperspectral sensor	NIR	-